

# FINITE VOLUME LEAST-SQUARES NEURAL NETWORK (FV-LSNN) METHOD FOR SCALAR NONLINEAR HYPERBOLIC CONSERVATION LAWS\*

ZHIQIANG CAI<sup>†</sup>, JINGSHUANG CHEN<sup>†</sup>, AND MIN LIU<sup>‡</sup>

**Abstract.** In [4], we introduced the least-squares ReLU neural network (LSNN) method for solving the linear advection-reaction problem with discontinuous solution and showed that the number of degrees of freedom for the LSNN method is significantly less than that of traditional mesh-based methods. The LSNN method is a discretization of an equivalent least-squares (LS) formulation in the class of neural network functions with the ReLU activation function; and evaluation of the LS functional is done by using numerical integration and proper numerical differentiation.

By developing a novel finite volume approximation (FVA) to the divergence operator, this paper studies the LSNN method for scalar nonlinear hyperbolic conservation laws. The FVA introduced in this paper is tailored to the LSNN method and is more accurate than traditional, well-studied FV schemes used in mesh-based numerical methods. Numerical results of some benchmark test problems with both convex and non-convex fluxes show that the finite volume LSNN (FV-LSNN) method is capable of computing the physical solution for problems with rarefaction waves and capturing the shock of the underlying problem automatically through the *free* hyper-planes of the ReLU neural network. Moreover, the method does not exhibit the common Gibbs phenomena along the discontinuous interface.

**Key words.** Finite Volume Scheme, Least-Squares Method, ReLU Neural Network, Scalar Nonlinear Hyperbolic Conservation Law

**AMS subject classifications.**

**1. Introduction.** Numerical approximations to solutions of nonlinear hyperbolic conservation laws (HCLs) are computationally challenging. Partly, this is because solutions of HCLs are often discontinuous due to discontinuous initial condition or shock formation; moreover, locations of the discontinuities are unknown for shock problems. Approximations to a discontinuous function with unknown discontinuous interfaces on fixed, quasi-uniform meshes are in general not accurate or exhibit unacceptable oscillations near a discontinuity. To overcome this obstacle, finite difference and finite volume methods often use higher order schemes with numerical techniques such as limiters, filters, ENO/WENO, etc. [13, 14, 15, 20]; and finite element methods usually employ discontinuous finite elements [2, 8, 11] and/or adaptive mesh refinement (AMR) to generate locally refined elements along discontinuous interfaces (see, e.g., [3, 16, 17]).

Neural networks (NNs) as a new class of functions have been used recently for solving partial differential equations (see, e.g., [7, 22, 26]) due to their expressive power. One of the striking features of NNs is the free hyper-planes implicitly generated by neurons that can automatically adapt to the target function and the solution of a PDE. This implies that the major numerical difficulty, when using *continuous* piece-wise polynomials to approximate a *discontinuous* function on a fixed, quasi-uniform mesh, can be overcome by NN functions. This fact was observed, used, and analyzed in [4] for solving linear advection-reaction problem with discontinuous solution. Specifically, applying the least-squares principle to the underlying problem studied in ([1, 9]) and using the ReLU neural network as the approximation class of functions, the least-squares neural network (LSNN) method was developed and studied in [4]. Compared to various AMR methods that locate the discontinuous interface through local mesh refinement process, the LSNN method is much more effective in terms of the number of degrees of freedom.

---

\*This work was supported in part by the National Science Foundation under grant DMS-2110571.

<sup>†</sup>Department of Mathematics, Purdue University, 150 N. University Street, West Lafayette, IN 47907-2067 (caiz@purdue.edu, chen2042@purdue.edu).

<sup>‡</sup>School of Mechanical Engineering, Purdue University, 585 Purdue Mall, West Lafayette, IN 47907-2088(liu66@purdue.edu).

The purpose of this paper is to study the space-time LSNN method for solving scalar HCLs. To do so, the first task is to determine a proper least-squares formulation. It is well-known that the differential form of a HCL is not generally sufficient to determine the solution and that an additional constraint, the so-called Rankine-Hugoniot (RH) relation [12, 20, 27], is needed at where solution is not continuous. This fact suggests that it is necessary to enforce the RH relation when discretizing the HCL.

For the inviscid Burgers equation, a least-squares formulation was developed to enforce the RH relation weakly by introducing the spatial-temporal flux as an independent variable in [10]; a variant of this method was also studied in [10, 18] by using the Helmholtz decomposition of the flux. Least-squares methods of this type have an additional term in the corresponding functionals comparing to the direct application of the least-squares principle to the original PDE. When using NNs instead of finite elements, we encounter some difficulties in training by the method of gradient descent and its variants.

To deal with this training issue, in [5] we employed the simple least-squares method used for the linear advection-reaction problem [4], i.e., a direct application of least-squares principle to the PDE and the initial condition. The RH relation is then enforced approximately through the discretization of the divergence operator by following ideas of the conservative schemes such as Roe's scheme, ENO, etc. Additionally, block space-time LSNN was introduced for problems with sharp changes in order to secure success of iterative solvers for the resulting non-convex optimization. Numerical results in [5] for the inviscid Burgers equation are promising but inaccurate for complicated initial condition; moreover, the method has limitations for problems with rarefaction waves and with non-convex spatial fluxes.

Well-studied conservative schemes such as Roe's scheme, ENO, WENO, etc. (see, e.g., [23, 24, 25]) were developed in the context of fixed, tensor-product meshes, and they are explicit in nature. This explains why a big effort in developing them was devoted to on how to approximate the spatial flux accurately and on using grid points possibly only on one side of discontinuous interfaces. Due to the implicit and mesh-less nature of the LSNN method, in this paper we introduce and study a new, accurate finite volume approximation (FVA) to the divergence operator, tailored to the LSNN method. The FVA is defined as an approximation to the average value of the divergence operator over each control volume; by the Gauss divergence theorem, the average value can be represented by boundary integrals that are further approximated by the composite trapezoidal or mid-point rule. The resulting FVA enforces the RH relation weakly and approximates the equation more accurately than existing conservative schemes; moreover, when the solution is discontinuous, its accuracy may be guaranteed by using enough boundary integration points (see Lemma 3.3).

The finite volume LSNN (FV-LSNN) method to be studied in this paper is again based on the simple least-squares method as in [5] and uses the newly developed FVA to approximate the divergence operator. It is shown that the residual of the FV-LSNN approximation is bounded by the best approximation of the class of NN functions in some measure (see Lemma 4.1) plus the approximation error of numerical integration and differentiation (see Lemma 4.2). Numerical results for the inviscid Burgers equation with various initial conditions show that the FV-LSNN method is able to compute the physical solution and to capture shock without oscillation, and is much more accurate than the LSNN method using existing conservative schemes. Moreover, it works well for the problem with a non-convex flux  $f(u) = u^3/3$ .

The paper is organized as follows. Section 2 describes the hyperbolic conservation law, its least-squares formulation, and preliminaries. The new finite volume schemes and their error bounds are introduced and analyzed in section 3 and appendix, respectively. The space-time finite volume LSNN method and its block version are presented in sections 4 and 5, respectively. Finally, numerical results for various benchmark test problems are given in section 6.

**2. Problem Formulation.** Let  $\tilde{\Omega}$  be a bounded domain in  $\mathbb{R}^d$  ( $d = 1, 2, \text{ or } 3$ ) with Lipschitz boundary, and  $I = (0, T)$  be the temporal interval. Consider the scalar nonlinear hyperbolic

conservation law

$$(2.1) \quad \begin{cases} u_t(\mathbf{x}, t) + \nabla_{\mathbf{x}} \cdot \tilde{\mathbf{f}}(u) = 0, & \text{in } \tilde{\Omega} \times I, \\ u = \tilde{g}, & \text{on } \tilde{\Gamma}_-, \\ u(\mathbf{x}, 0) = u_0(\mathbf{x}), & \text{in } \tilde{\Omega}, \end{cases}$$

where  $u_t$  is the partial derivative of  $u$  with respect to the temporal variable  $t$ ;  $\nabla_{\mathbf{x}} \cdot$  is a divergence operator with respect to the spatial variable  $\mathbf{x}$ ;  $\tilde{\mathbf{f}}(u) = (f_1(u), \dots, f_d(u))$  is the spatial flux vector field;  $\tilde{\Gamma}_-$  is the part of the boundary  $\partial\tilde{\Omega} \times I$  where the characteristic curves enter the domain  $\tilde{\Omega} \times I$ ; and the boundary data  $\tilde{g}$  and the initial data  $u_0$  are given scalar-valued functions. Without loss of generality, assume that  $f_i(u)$  is twice differentiable for  $i = 1, \dots, d$ .

Problem (2.1) is a hyperbolic partial differential equation defined on a space-time domain  $\Omega = \tilde{\Omega} \times I$  in  $\mathbb{R}^{d+1}$ . Denote the inflow boundary of the domain  $\Omega$  and the inflow boundary condition by

$$\Gamma_- = \begin{cases} \tilde{\Gamma}_-, & t \in (0, T), \\ \Omega, & t = 0 \end{cases} \quad \text{and} \quad g = \begin{cases} \tilde{g}, & \text{on } \tilde{\Gamma}_-, \\ u_0(\mathbf{x}), & \text{on } \Omega, \end{cases}$$

respectively. Then (2.1) may be rewritten as the following compact form

$$(2.2) \quad \begin{cases} \nabla \cdot \mathbf{f}(u) = 0, & \text{in } \Omega \in \mathbb{R}^{d+1}, \\ u = g, & \text{on } \Gamma_-, \end{cases}$$

where  $\nabla \cdot = (\nabla_{\mathbf{x}} \cdot, \partial_t)$  is a divergence operator with respect to both spatial and temporal variables  $\mathbf{z} = (\mathbf{x}, t)$ , and  $\mathbf{f}(u) = (f_1(u), \dots, f_d(u), u) = (\tilde{\mathbf{f}}(u), u)$  is the spatial and temporal flux vector field. Assume that  $u \in L^\infty(\Omega)$ . Then  $u$  is called a weak solution of (2.2) if and only if

$$(2.3) \quad -(\mathbf{f}(u), \nabla \varphi)_{0, \Omega} + (\mathbf{n} \cdot \mathbf{f}(u), \varphi)_{0, \Gamma_-} = 0, \quad \forall \varphi \in C_{\Gamma_+}^1(\bar{\omega}),$$

where  $\Gamma_+ = \partial\Omega \setminus \Gamma_-$  is the outflow boundary and  $C_{\Gamma_+}^1(\bar{\omega}) = \{\varphi \in C^1(\bar{\omega}) : \varphi = 0 \text{ on } \Gamma_+\}$ .

Denote the collection of square integrable vector fields whose divergence is also square integrable by

$$H(\text{div}; \Omega) = \{\boldsymbol{\tau} \in L^2(\Omega)^{d+1} \mid \nabla \cdot \boldsymbol{\tau} \in L^2(\Omega)\}.$$

It is then easy to see that solutions of (2.2) are in the following subset of  $L^2(\Omega)$

$$V_{\mathbf{f}} = \{v \in L^2(\Omega) \mid \mathbf{f}(v) \in H(\text{div}; \Omega)\}.$$

Define the least-squares (LS) functional

$$(2.4) \quad \mathcal{L}(v; g) = \|\nabla \cdot \mathbf{f}(v)\|_{0, \Omega}^2 + \|v - g\|_{0, \Gamma_-}^2,$$

where  $\|\cdot\|_{0, S}$  denotes the standard  $L^2(S)$  norm for  $S = \Omega$  and  $\Gamma_-$ . Now, the corresponding least-squares formulation is to seek  $u \in V_{\mathbf{f}}$  such that

$$(2.5) \quad \mathcal{L}(u; g) = \min_{v \in V_{\mathbf{f}}} \mathcal{L}(v; g).$$

**PROPOSITION 2.1.** *Assume that  $u \in L^\infty(\Omega)$  is a piece-wise  $C^1$  function. Then  $u$  is a weak solution of (2.2) if and only if  $u$  is a solution of the minimization problem in (2.5).*

*Proof.* The proposition is a direct consequence of Theorem 2.5 in [10].  $\square$

**3. Finite Volume Approximation.** As seen in [4, 5], discretization of the differential operator is critical for the success of the LSNN method. The simple finite difference quotient along coordinate directions generally results in a very poor numerical approximation even in the linear case when the solution is not continuous. This is because such a simple finite difference quotient does not satisfy the well-known Rankine-Hugoniot (RH) relation [20, 14] near the discontinuous interface.

To overcome this difficulty, many conservative schemes on tensor-product meshes such as Roe's scheme, ENO, WENO, etc. (see, e.g., [23, 24, 25]) have been well developed and studied. These conservative schemes are based on the finite volume approximation to the divergence equation. In this way, the RH relation is automatically enforced. Additional ingredient of the methods is to use grid points, if possible, only on one side of the discontinuous interfaces for approximating the spatial flux. Due to the implicit and mesh-less nature of the LSNN method, in this section we introduce new finite volume approximations to the divergence operator in  $\mathbb{R}^{d+1}$ , tailored to the LSNN method.

**3.1. One Dimension.** For clarity of presentation, let us first consider the one dimensional case with  $\Omega = (a, b) \times (0, T)$ . Partition the domain  $\Omega$  by a uniform mesh:

$$a = x_0 < x_1 < \cdots < x_m = b \quad \text{and} \quad 0 = t_0 < t_1 < \cdots < t_n = T$$

with  $x_i = a + ih$  and  $t_j = j\tau$ , where  $h = (b - a)/m$  and  $\tau = T/n$  are the mesh sizes in the respective space and time. For  $i = 0, 1, \dots, m - 1$  and  $j = 0, 1, \dots, n - 1$ , denote the control volumes and their centroids by

$$K_{ij} = (x_i, x_{i+1}) \times (t_j, t_{j+1}) \quad \text{and} \quad \mathbf{m}_{ij} = (x_i + h/2, t_j + \tau/2),$$

respectively.

To simplify notations, we also introduce the following generic notations. Denote this uniform partition of the domain  $\Omega$  by

$$\mathcal{T} = \{K = K_{ij} : i = 0, 1, \dots, m - 1; j = 0, 1, \dots, n - 1\},$$

and the centroid of element  $K \in \mathcal{T}$  by  $\mathbf{m}_K$ . For a function  $\varphi$  defined in  $\Omega$ , let  $\text{avg}_{\mathcal{T}}(\varphi)$  be a piece-wise constant function with respect to the partition  $\mathcal{T}$  such that its restriction over element  $K \in \mathcal{T}$  is given by

$$\text{avg}_{\mathcal{T}}(\varphi)|_K = \text{avg}_K(\varphi) = \frac{1}{|K|} \int_K \varphi(\mathbf{z}) \, d\mathbf{z}.$$

In one dimension, the space-time flux is the two-dimensional vector field  $\mathbf{f}(u) = (f(u), u)$ . For simplicity of notation, let  $\sigma = f(u)$  and  $\mathbf{f}(u) = (\sigma, u)$ . Then using the Gauss divergence theorem, we have

$$\begin{aligned} \text{avg}(\nabla \cdot \mathbf{f}(u))|_{K_{ij}} &= \text{avg}_{K_{ij}}(\nabla \cdot \mathbf{f}(u)) = \frac{1}{|K_{ij}|} \int_{\partial K_{ij}} \mathbf{n} \cdot \mathbf{f}(u) \, ds \\ (3.1) \quad &= \frac{1}{|K_{ij}|} \int_{t_j}^{t_{j+1}} (\sigma(x_{i+1}, t) - \sigma(x_i, t)) \, dt + \frac{1}{|K_{ij}|} \int_{x_i}^{x_{i+1}} (u(x, t_{j+1}) - u(x, t_j)) \, dx. \end{aligned}$$

Since  $u$  and hence  $\sigma$  may be discontinuous on the boundary of  $K_{ij}$ , we use a composite lower order, instead of higher order, quadrature rule such as the composite trapezoidal or mid-point rule for approximating the boundary integrals in (3.1). To this end, partition the intervals  $[x_i, x_{i+1}]$  and  $[t_j, t_{j+1}]$  into uniform sub-intervals

$$x_i = x_i^0 < x_i^1 < \cdots < x_i^{\hat{m}} = x_{i+1} \quad \text{and} \quad t_j = t_j^0 < t_j^1 < \cdots < t_j^{\hat{n}} = t_{j+1},$$

respectively, where  $x_i^k = x_i + k\hat{h}$  and  $t_j^k = t_j + k\hat{\tau}$ , and  $\hat{h} = h/\hat{m}$  and  $\hat{\tau} = \tau/\hat{n}$  are the numerical integration mesh sizes. Then the finite volume approximation to the divergence operator at the mid-point  $\mathbf{m}_{K_{ij}}$  of the control volume  $K_{ij}$  based on the composite trapezoidal rule is given by

$$(3.2) \quad \begin{aligned} & \nabla_{\tau}^t \cdot \mathbf{f}(u(\mathbf{m}_{K_{ij}})) \\ &= \frac{\hat{\tau}}{2h\tau} \left\{ (\sigma(x_{i+1}, t_j) - \sigma(x_i, t_j)) + 2 \sum_{k=1}^{\hat{n}-1} (\sigma(x_{i+1}, t_j^k) - \sigma(x_i, t_j^k)) + (\sigma(x_{i+1}, t_{j+1}) - \sigma(x_i, t_{j+1})) \right\} \\ &+ \frac{\hat{h}}{2h\tau} \left\{ (u(x_i, t_{j+1}) - u(x_i, t_j)) + 2 \sum_{k=1}^{\hat{m}-1} (u(x_i^k, t_{j+1}) - u(x_i^k, t_j)) + (u(x_{i+1}, t_{j+1}) - u(x_{i+1}, t_j)) \right\}. \end{aligned}$$

Denote the mid-points by

$$x_i^{k-1/2} = x_i + (k-1/2)\hat{h} \quad \text{and} \quad t_j^{k-1/2} = t_j + (k-1/2)\hat{\tau}.$$

The finite volume approximation to the divergence operator at the point  $\mathbf{m}_{K_{ij}}$  of the control volume  $K_{ij}$  based on the composite mid-point rule is given by

$$(3.3) \quad \begin{aligned} \nabla_{\tau}^m \cdot \mathbf{f}(u)|_{K_{ij}} &= \nabla_{\tau}^m \cdot \mathbf{f}(u(\mathbf{m}_{K_{ij}})) = \frac{\hat{\tau}}{h\tau} \sum_{k=1}^{\hat{n}} (\sigma(x_{i+1}, t_j^{k-1/2}) - \sigma(x_i, t_j^{k-1/2})) \\ &+ \frac{\hat{h}}{h\tau} \sum_{k=1}^{\hat{m}} (u(x_i^{k-1/2}, t_{j+1}) - u(x_i^{k-1/2}, t_j)). \end{aligned}$$

REMARK 3.1. Denote by  $u_{i,j}$  as approximation to  $u(x_i, t_j)$ . (3.2) with  $\hat{m} = \hat{n} = 1$  leads to the following implicit finite volume scheme for the one-dimensional scalar nonlinear HCL:

$$(3.4) \quad \frac{u_{i+1,j+1} + u_{i,j+1}}{\tau} + \frac{f(u_{i+1,j+1}) - f(u_{i,j+1})}{h} = \frac{u_{i+1,j} + u_{i,j}}{\tau} - \frac{f(u_{i+1,j}) - f(u_{i,j})}{h}$$

for  $i = 0, 1, \dots, m-1$  and  $j = 0, 1, \dots, n-1$ .

Below, we state error estimates of the finite volume approximations to the average of the divergence of the total flux and postpone their proof to Appendix.

LEMMA 3.2. Assume that  $u$  is a  $C^2$  function in  $K_{ij} \in \mathcal{T}$  and that  $f(u)$  is a  $C^2$  function. For  $\text{int} = t, m$ , there exists a constant  $C > 0$  such that

$$(3.5) \quad \|\nabla_{\tau}^{\text{int}} \cdot \mathbf{f}(u) - \text{avg}(\nabla \cdot \mathbf{f}(u))\|_{L^p(K_{ij})} \leq C \left( \frac{\tau^2}{\hat{n}^2 h^{1/q}} + \frac{h^2}{\hat{m}^2 \tau^{1/q}} \right).$$

This lemma indicates that  $\hat{m} = 1$  and  $\hat{n} = 1$  are sufficient for problems with smooth solution. It is more complicated when  $u$  is discontinuous on the boundary of  $K_{ij}$ . Next lemma states an estimate in one of three cases which will be proved in Appendix.

LEMMA 3.3. Assume that  $f(u)$  is a  $C^2$  function and that  $u$  is a piece-wise  $C^2$  function on the boundary of  $K_{ij}$ . Moreover, assume that  $u$  has one jump discontinuity at each of two horizontal boundary edges,  $t = t_j$  and  $t = t_{j+1}$ , of  $K_{ij}$ , and let  $\delta_l^x \in (x_i^{k_l}, x_i^{k_l+1})$  for  $l = j, j+1$ . Then for  $\text{int} = t, m$ , there exists a constant  $C > 0$  such that

$$(3.6) \quad \begin{aligned} & \|\nabla_{\tau}^{\text{int}} \cdot \mathbf{f}(u) - \text{avg}(\nabla \cdot \mathbf{f}(u))\|_{L^p(K_{ij})} \leq C \left( \frac{\tau^2}{\hat{n}^2 h^{1/q}} + \frac{h^2}{\hat{m}^2 \tau^{1/q}} \right) \\ &+ C \frac{h}{\hat{m}^{1+1/q} \tau^{1/q}} \sum_{l=j}^{j+1} \|u_x(\cdot, t_l)\|_{L^p((x_i^{k_l}, x_i^{k_l+1}) \setminus \{\delta_l^x\})} + \sum_{l=j}^{j+1} (\delta_l^x - x_i^{k_l}) \llbracket u(\delta_l^x, t_l) \rrbracket, \end{aligned}$$

where  $\llbracket u(\delta_l^x, t_l) \rrbracket$  is the jump of  $u$  at  $(\delta_l^x, t_l)$ .

REMARK 3.4. Notice that  $\delta_l^x - x_i^{k_l} \leq h/\hat{m}$ . Lemma 3.3 suggests that the choice of  $\hat{m}$  or/and  $\hat{n}$  depending on the jump of the solution, when  $u$  is discontinuous on the boundary of  $K_{ij}$ .

REMARK 3.5. Error bounds similar to (3.6) hold for the other cases that  $\Gamma_{ij}$  intercepts (i) two horizontal edges or (ii) one horizontal and one vertical edges of  $K_{ij}$ . The first term on the left-hand side of (3.6) remains unchanged, and the second term is replaced by a constant  $C$  multiplied by

$$\frac{\tau}{\hat{n}^{1+1/q} h^{1/q}} \sum_{l=i}^{i+1} \|\sigma_t(x_l, \cdot)\|_{L^p((t_j^{k_l}, t_j^{k_{l+1}}) \setminus \{\delta_l^t\})} + \sum_{l=i}^{i+1} (\delta_l^t - t_j^{k_l}) \llbracket \sigma(x_l, \delta_l^t) \rrbracket$$

for the case (i) and by

$$\begin{aligned} & \frac{h}{\hat{m}^{1+1/q} \tau^{1/q}} \sum_{l=j}^{j+1} \|u_x(\cdot, t_l)\|_{L^p((x_i^{k_l}, x_i^{k_{l+1}}) \setminus \{\delta_l^x\})} + \sum_{l=j}^{j+1} (\delta_l^x - x_i^{k_l}) \llbracket u(\delta_l^x, t_l) \rrbracket \\ & + \frac{\tau}{\hat{n}^{1+1/q} h^{1/q}} \sum_{l=i}^{i+1} \|\sigma_t(x_l, \cdot)\|_{L^p((t_j^{k_l}, t_j^{k_{l+1}}) \setminus \{\delta_l^t\})} + \sum_{l=i}^{i+1} (\delta_l^t - t_j^{k_l}) \llbracket \sigma(x_l, \delta_l^t) \rrbracket \end{aligned}$$

for the case (ii).

**3.2. Two Dimensions.** In this section, we describe the finite volume approximations to the divergence operator based on the composite trapezoidal and mid-point rules in two dimensions. Extensions to three dimensions are straightforward.

Let  $\Omega = \tilde{\Omega} \times I = (a_1, b_1) \times (a_2, b_2) \times (0, T)$ . Uniformly partition the domain  $\tilde{\Omega} = (a_1, b_1) \times (a_2, b_2)$  by

$$a_1 = x_0 < x_1 < \cdots < x_{m_1} = b_1 \quad \text{and} \quad a_2 = y_0 < y_1 < \cdots < y_{m_2} = b_2$$

and the interval  $I = (0, T)$  by  $0 = t_0 < t_1 < \cdots < t_n = T$  with  $x_i = a_1 + ih_1$ ,  $y_j = a_2 + jh_2$ , and  $t_k = j\tau$ , where  $h_l = (b_l - a_l)/m_l$  for  $l = 1, 2$  and  $\tau = T/n$  are the mesh sizes in the respective space and time. For  $i = 0, 1, \dots, m_1 - 1$ ,  $j = 0, 1, \dots, m_2 - 1$  and  $k = 0, 1, \dots, n - 1$ , denote the control volumes and their mid-points by

$$(3.7) \quad K_{ijk} = (x_i, x_{i+1}) \times (y_j, y_{j+1}) \times (t_k, t_{k+1}) \quad \text{and} \quad \mathbf{m}_{ijk} = (x_i + h_1/2, y_j + h_2/2, t_k + \tau/2),$$

respectively. Let  $\boldsymbol{\sigma} = (f_1(u), f_2(u))$ , then the space-time flux is the three-dimensional vector field:  $\mathbf{f}(u) = (\boldsymbol{\sigma}, u) = (\sigma_1, \sigma_2, u)$ . Using the Gauss divergence theorem, we have

$$(3.8) \quad \begin{aligned} \int_{K_{ijk}} \nabla \cdot \mathbf{f}(u) \, dz &= \int_{\partial K_{ijk}} \mathbf{n} \cdot \mathbf{f}(u) \, dS = \tau \int_{x_i}^{x_{i+1}} \int_{y_j}^{y_{j+1}} u(x, y; t_{k+1}, t_k) \, dy dx \\ &+ h_1 \int_{t_k}^{t_{k+1}} \int_{y_j}^{y_{j+1}} \sigma_1(y, t; x_{i+1}, x_i) \, dy dt + h_2 \int_{t_k}^{t_{k+1}} \int_{x_i}^{x_{i+1}} \sigma_2(x, t; y_{j+1}, y_j) \, dx dt, \end{aligned}$$

where the integrands,  $u(x, y; t_{k+1}, t_k)$ ,  $\sigma_1(y, t; x_{i+1}, x_i)$ ,  $\sigma_2(x, t; y_{j+1}, y_j)$ , are divided differences with respect to  $t$ ,  $x$ , and  $y$ , respectively, and are defined by

$$\sigma_1(y, t; x_{i+1}, x_i) = \frac{\sigma_1(x_{i+1}, y, t) - \sigma_1(x_i, y, t)}{h_1}, \quad \sigma_2(x, t; y_{j+1}, y_j) = \frac{\sigma_2(x, y_{j+1}, t) - \sigma_2(x, y_j, t)}{h_2},$$

$$\text{and} \quad u(x, y; t_{k+1}, t_k) = \frac{u(x, y, t_{k+1}) - u(x, y, t_k)}{\tau}.$$

Uniformly partition the intervals  $[x_i, x_{i+1}]$ ,  $[y_j, y_{j+1}]$ , and  $[t_k, t_{k+1}]$  by

$$x_i = x_i^0 < x_i^1 < \dots < x_i^{\hat{m}_1} = x_{i+1}, \quad y_j = y_j^0 < y_j^1 < \dots < y_j^{\hat{m}_2} = y_{j+1},$$

$$\text{and } t_k = t_k^0 < t_k^1 < \dots < t_k^{\hat{n}} = t_{k+1},$$

respectively, where  $x_i^l = x_i + l\hat{h}_1$ ,  $y_j^l = y_j + l\hat{h}_2$ , and  $t_k^l = t_k + l\hat{\tau}$ ; and  $\hat{h}_1 = h_1/\hat{m}_1$ ,  $\hat{h}_2 = h_2/\hat{m}_2$ , and  $\hat{\tau} = \tau/\hat{n}$  are the numerical integration mesh sizes. Denote the mid-points by

$$x_i^{l-1/2} = x_i + (l-1/2)\hat{h}_1, \quad y_j^{l-1/2} = y_j + (l-1/2)\hat{h}_2, \quad \text{and } t_k^{l-1/2} = t_k + (l-1/2)\hat{\tau}.$$

Let  $\mathbf{h} = (h_1, h_2)$ . Then by (3.8), the finite volume approximations to the divergence operator at the mid-point  $\mathbf{m}_{ijk}$  of the control volume  $K_{ijk}$  are given by

$$(3.9) \quad \begin{aligned} \nabla_{(\mathbf{h}, \tau)}^p \cdot \mathbf{f}(u(\mathbf{m}_{ijk})) &= \frac{1}{4\tau\hat{m}_1\hat{m}_2} \sum_{l_1=0}^{\hat{m}_1-1} \sum_{l_2=0}^{\hat{m}_2-1} \sum_{p,q=0}^1 u(x_i^{l_1+p}, y_j^{l_2+q}, t_{k+1}, t_k) \\ &+ \frac{1}{4h_1\hat{m}_2\hat{n}} \sum_{l=0}^{\hat{n}-1} \sum_{l_2=0}^{\hat{m}_2-1} \sum_{p,q=0}^1 \sigma_1(y_j^{l_2+p}, t_k^{l+q}, x_{i+1}, x_i) + \frac{1}{4h_2\hat{m}_1\hat{n}} \sum_{l=0}^{\hat{n}-1} \sum_{l_1=0}^{\hat{m}_1-1} \sum_{p,q=0}^1 \sigma_2(x_i^{l_1+p}, t_k^{l+q}, y_{j+1}, y_j) \end{aligned}$$

based on the composite trapezoidal rule and by

$$(3.10) \quad \begin{aligned} \nabla_{(\mathbf{h}, \tau)}^m \cdot \mathbf{f}(u(\mathbf{m}_{ijk})) &= \frac{1}{\tau\hat{m}_1\hat{m}_2} \sum_{l_1=1}^{\hat{m}_1} \sum_{l_2=1}^{\hat{m}_2} u(x_i^{l_1-1/2}, y_j^{l_2-1/2}, t_{k+1}, t_k) \\ &+ \frac{1}{h_1\hat{m}_2\hat{n}} \sum_{l=1}^{\hat{n}} \sum_{l_2=1}^{\hat{m}_2} \sigma_1(y_j^{l_2-1/2}, t_k^{l-1/2}, x_{i+1}, x_i) + \frac{1}{h_2\hat{m}_1\hat{n}} \sum_{l=1}^{\hat{n}} \sum_{l_1=1}^{\hat{m}_1} \sigma_2(x_i^{l_1-1/2}, t_k^{l-1/2}, y_{j+1}, y_j) \end{aligned}$$

based on the composite mid-point rule.

**4. Space-Time FV-LSNN Method.** In this section, we describe the finite volume least-squares neural network (FV-LSNN) method for the scalar hyperbolic conservation law.

A deep neural network (DNN) defines a scalar-valued function

$$\mathcal{N} : \mathbf{z} = (\mathbf{x}, t) \in \mathbb{R}^{d+1} \longrightarrow \mathcal{N}(\mathbf{z}) \in \mathbb{R}.$$

A DNN function  $\mathcal{N}(\mathbf{z})$  is typically represented as compositions of many layers of functions:

$$(4.1) \quad \mathcal{N}(\mathbf{z}) = \boldsymbol{\omega}^{(L)} \left( N^{(L-1)} \circ \dots \circ N^{(2)} \circ N^{(1)}(\mathbf{z}) \right) - b^{(L)},$$

where  $\boldsymbol{\omega}^{(L)} \in \mathbb{R}^{n_L-1}$ ,  $b^{(L)} \in \mathbb{R}$ , the symbol  $\circ$  denotes the composition of functions, and  $L$  is the depth of the network. For  $l = 1, \dots, L-1$ , the  $N^{(l)} : \mathbb{R}^{n_{l-1}} \rightarrow \mathbb{R}^{n_l}$  is called the  $l^{\text{th}}$  hidden layer of the network defined as follows:

$$(4.2) \quad N^{(l)}(\mathbf{z}^{(l-1)}) = \sigma(\boldsymbol{\omega}^{(l)} \mathbf{z}^{(l-1)} - \mathbf{b}^{(l)}) \quad \text{for } \mathbf{z}^{(l-1)} \in \mathbb{R}^{n_{l-1}},$$

where  $\boldsymbol{\omega}^{(l)} \in \mathbb{R}^{n_l \times n_{l-1}}$ ,  $\mathbf{b}^{(l)} \in \mathbb{R}^{n_l}$ ,  $\mathbf{z}^{(0)} = \mathbf{z}$ , and  $\sigma$  is the activation function and its application to a vector is defined component-wisely. This paper will use the popular rectified linear unit (ReLU) activation function defined by

$$(4.3) \quad \sigma(t) = \max\{0, t\} = \begin{cases} 0, & \text{if } t \leq 0, \\ t, & \text{if } t > 0. \end{cases}$$

Denote the set of DNN functions by

$$\mathcal{M}_N(\boldsymbol{\theta}, L) = \left\{ \mathcal{N}(\mathbf{z}) = \boldsymbol{\omega}^{(L)} \left( N^{(L-1)} \circ \dots \circ N^{(2)} \circ N^{(1)}(\mathbf{z}) \right) - \mathbf{b}^{(L)} : \boldsymbol{\omega}^{(l)} \in \mathbb{R}^{n_l \times n_{l-1}}, \mathbf{b}^{(l)} \in \mathbb{R}^{n_l} \right\},$$

where  $N^{(l)}(\mathbf{z}^{(l-1)})$  is defined in (4.2) and  $\boldsymbol{\theta}$  denotes all parameters:  $\boldsymbol{\omega}^{(l)}$  and  $\mathbf{b}^{(l)}$  for  $l = 1, \dots, L$ . It is easy to see that  $\mathcal{M}(\boldsymbol{\theta}, L)$  is a subset of  $V_{\mathbf{f}}$ , but not a linear subspace. The least-squares approximation is to find  $u^N(\mathbf{z}; \boldsymbol{\theta}^*) \in \mathcal{M}_N(\boldsymbol{\theta}, L)$  such that

$$(4.4) \quad \mathcal{L}(u^N(\cdot; \boldsymbol{\theta}^*); g) = \min_{v \in \mathcal{M}_N(\boldsymbol{\theta}, L)} \mathcal{L}(v(\cdot; \boldsymbol{\theta}); g) = \min_{\boldsymbol{\theta} \in \mathbb{R}^N} \mathcal{L}(v(\cdot; \boldsymbol{\theta}); g),$$

where  $N$  is the total number of parameters in  $\mathcal{M}_N(\boldsymbol{\theta}, L)$  given by

$$N = M_d(L) = \sum_{l=1}^L n_l \times (n_{l-1} + 1).$$

LEMMA 4.1. *Let  $u$  be the solution of (2.2), and let  $u^N \in \mathcal{M}_N \equiv \mathcal{M}_N(\boldsymbol{\theta}, L)$  be a solution of (4.4). There exists a positive constant  $C$  such that*

$$(4.5) \quad \begin{aligned} \mathcal{L}(u^N; g) &= \inf_{v \in \mathcal{M}_N} \left( \|v - u\|_{0, \Gamma_-}^2 + \|\nabla \cdot [\mathbf{f}(v) - \mathbf{f}(u)]\|_{0, \Omega}^2 \right) \\ &\leq C \inf_{v \in \mathcal{M}_N} \left( \|v - u\|_{0, \Gamma_-}^2 + \|\nabla \cdot [\mathbf{f}'(u)(v - u)]\|_{0, \Omega}^2 \right) + h.o.t., \end{aligned}$$

where *h.o.t.* means a higher order term comparing to the first term.

*Proof.* For any  $v \in \mathcal{M}_N(\boldsymbol{\theta}, L)$ , (4.4) and (2.2) imply that

$$\mathcal{L}(u^N; g) \leq \mathcal{L}(v; g) = \|v - u\|_{0, \Gamma_-}^2 + \|\nabla \cdot [\mathbf{f}(v) - \mathbf{f}(u)]\|_{0, \Omega}^2,$$

which proves the validity of the equality in (4.5). By the Taylor expansion, there exists a  $w$  between  $u$  and  $v$  such that

$$\mathbf{f}(v) - \mathbf{f}(u) = \mathbf{f}'(u)(v - u) + \frac{1}{2} \mathbf{f}''(w)(v - u)^2,$$

where  $\mathbf{f}'(u) = (\tilde{\mathbf{f}}'(u), 1)^t$  and  $\mathbf{f}''(u) = (\tilde{\mathbf{f}}''(u), 0)^t$ . Together with the triangle inequality we have

$$(4.6) \quad \|\nabla \cdot [\mathbf{f}(v) - \mathbf{f}(u)]\|_{0, \Omega} \leq \|\nabla \cdot [\mathbf{f}'(u)(v - u)]\|_{0, \Omega} + \frac{1}{2} \|\nabla \cdot [\mathbf{f}''(w)(v - u)^2]\|_{0, \Omega}.$$

Notice that the second term in the right-hand side of (4.6) is a higher order term comparing to the first term. Now, the inequality in (4.5) is a direct consequence of the equality in (4.5) and (4.6). This completes the proof of the lemma.  $\square$

REMARK 4.2. *When  $u$  is sufficiently smooth, the second term  $\nabla \cdot [\mathbf{f}'(u)(v - u)] = (v - u) \nabla \cdot \mathbf{f}'(u) + \mathbf{f}'(u) \cdot \nabla(v - u)$  may be bounded by the sum of the  $L^2$  norm of  $v - u$  and the  $L^2$  norm of the directional derivative of  $v - u$  along the direction  $\mathbf{f}'(u)$ .*

Evaluation of the least-squares functional  $\mathcal{L}(v; g)$  defined in (2.4) requires integration and differentiation over the computational domain and the inflow boundary. We approximate integration and differentiation by the composite mid-point rule similar to [7, 4] and the finite volume schemes introduced in Section 3, respectively.

For simplicity, we describe the discrete least-squares approximation in two dimensions and for the domain  $\Omega = (a_1, b_1) \times (a_2, b_2) \times (0, T) \in \mathbb{R}^{2+1}$ . To this end, denote a uniform partition of the domain  $\Omega$  by

$$\mathcal{T} = \{K = K_{ijk} : i = 0, 1, \dots, m_1 - 1; j = 0, 1, \dots, m_2 - 1; k = 0, 1, \dots, n - 1\},$$



where  $K_{ijk}$  is defined in (3.7). Then

$$\mathcal{E}_- = \{E = \partial K \cap \Gamma_- : K \in \mathcal{T}\}$$

is a partition of the inflow boundary  $\Gamma_-$ . Let  $\mathbf{z}_K$  and  $\mathbf{z}_E$  be the mid-points of  $K \in \mathcal{T}$  and  $E \in \mathcal{E}_-$ , respectively. Define the discrete LS functional as follows:

$$(4.7) \quad \mathcal{L}_\mathcal{T}(v(\cdot; \boldsymbol{\theta}); g) = \sum_{K \in \mathcal{T}} \left( \nabla_\mathcal{T} \cdot \mathbf{f}(v(\mathbf{z}_K; \boldsymbol{\theta})) \right)^2 |K| + \sum_{E \in \mathcal{E}_-} (v - g)^2(\mathbf{z}_E; \boldsymbol{\theta}) |E|,$$

where  $|K|$  and  $|E|$  denote the area of  $K$  and the length of  $E$ , respectively; and  $\nabla_\mathcal{T} \cdot$  is a discrete divergence operator defined in either (3.9) or (3.10). Now, the discrete least-squares approximation is to find  $u_\mathcal{T}^N(\mathbf{z}, \boldsymbol{\theta}^*) \in \mathcal{M}_N(\boldsymbol{\theta}, L)$  such that

$$(4.8) \quad \mathcal{L}_\mathcal{T}(u_\mathcal{T}^N(\cdot, \boldsymbol{\theta}^*); g) = \min_{v \in \mathcal{M}_N(\boldsymbol{\theta}, L)} \mathcal{L}_\mathcal{T}(v(\cdot; \boldsymbol{\theta}); g) = \min_{\boldsymbol{\theta} \in \mathbb{R}^N} \mathcal{L}_\mathcal{T}(v(\cdot; \boldsymbol{\theta}); g).$$

LEMMA 4.3. *Let  $u$ ,  $u_N$ , and  $u_\mathcal{T}^N$  be the solutions of problems (2.4), (4.4), and (4.8), respectively. Then we have*

$$(4.9) \quad \mathcal{L}(u_\mathcal{T}^N; g) \leq \left| (\mathcal{L} - \mathcal{L}_\mathcal{T})(u_\mathcal{T}^N; g) \right| + \left| (\mathcal{L} - \mathcal{L}_\mathcal{T})(u^N; g) \right| + \left| \mathcal{L}(u^N; g) \right|.$$

*Proof.* By the fact that  $\mathcal{L}_\mathcal{T}(u_\mathcal{T}^N; \mathbf{f}) \leq \mathcal{L}_\mathcal{T}(u_N; \mathbf{f})$ , we have

$$(4.10) \quad \begin{aligned} \mathcal{L}(u_\mathcal{T}^N; g) &= (\mathcal{L} - \mathcal{L}_\mathcal{T})(u_\mathcal{T}^N; g) + \mathcal{L}_\mathcal{T}(u_\mathcal{T}^N; g) \leq (\mathcal{L} - \mathcal{L}_\mathcal{T})(u_\mathcal{T}^N; g) + \mathcal{L}_\mathcal{T}(u^N; g) \\ &= (\mathcal{L} - \mathcal{L}_\mathcal{T})(u_\mathcal{T}^N; g) + (\mathcal{L}_\mathcal{T} - \mathcal{L})(u^N; g) + \mathcal{L}(u^N; g), \end{aligned}$$

which, together with the triangle inequality, implies (4.9).  $\square$

This lemma indicates that the minimum of the discrete least-squares functional  $\mathcal{L}_\mathcal{T}$  over  $\mathcal{M}_N(\boldsymbol{\theta}, L)$  is bounded by the minimum of the least-squares functional  $\mathcal{L}$  over  $\mathcal{M}_N(\boldsymbol{\theta}, L)$  plus the approximation error of numerical integration and differentiation in  $\mathcal{M}_N(\boldsymbol{\theta}, L)$ .

**5. Block Space-Time FV-LSNN Method.** Due to the difficulty of training the space-time LSNN method over a relative large computational domain  $\Omega$ , in [5] we proposed the block space-time LSNN method. The method is based on a partition,  $\{\Omega_i\}_{i=1}^{m_0}$ , of the computational domain  $\Omega = \tilde{\Omega} \times I$ , where the subdomains satisfy the following inclusion relation

$$\Omega_1 \subset \dots \subset \Omega_{m_0} = \Omega.$$

Moreover,  $\Omega_{i-1,i} = \Omega_i \setminus \Omega_{i-1}$  is in the range of influence of

$$\Gamma_{i-1,i} = \partial(\Omega_i \setminus \Omega_{i-1}) \cap \partial\Omega_{i-1} \quad \text{and} \quad \Gamma_-^i = \partial\Omega_{i-1,i} \cap (\Gamma_- \cup (\tilde{\Omega} \times \{0\})),$$

where  $\Omega_0 = \emptyset$ .

Denote by  $u_i = u|_{\Omega_i \setminus \Omega_{i-1}}$  the restriction of the solution  $u$  of (2.2) on  $\Omega_{i-1,i}$ , then  $u_i$  is the solution of the following problem:

$$(5.1) \quad \begin{cases} \nabla \cdot \mathbf{f}(u_i) = 0, & \text{in } \Omega_{i-1,i} \in \mathbb{R}^{d+1}, \\ u_i = u_{i-1}, & \text{on } \Gamma_{i-1,i}, \\ u_i = g, & \text{on } \Gamma_-^i \end{cases}$$

for  $i = 1, \dots, m_0$ .

Define the least-squares functional for problem (5.1) by

$$\mathcal{L}^i(v; u_{i-1}, g) = \|\nabla \cdot \mathbf{f}(v)\|_{0, \Omega_{i-1, i}}^2 + \|v - u_{i-1}\|_{0, \Gamma_{i-1, i}}^2 + \|v - g\|_{0, \Gamma_{i-}}^2.$$

Then the corresponding discrete least-squares functional  $\mathcal{L}_{\mathcal{T}}^i(v(\cdot; \boldsymbol{\theta}); u_{i-1}, g)$  over the subdomain  $\Omega_{i-1, i}$  may be defined in a similar fashion as in (4.7). Now, the block space-time LSNN method is to find  $u_{\mathcal{T}}^i(\mathbf{z}, \boldsymbol{\theta}_i^*) \in \mathcal{M}(\boldsymbol{\theta}, L)$  such that

$$(5.2) \quad \mathcal{L}_{\mathcal{T}}^i(u_{\mathcal{T}}^i(\cdot, \boldsymbol{\theta}_i^*); u_{i-1}, g) = \min_{v \in \mathcal{M}(\boldsymbol{\theta}, L)} \mathcal{L}_{\mathcal{T}}^i(v(\cdot; \boldsymbol{\theta}); u_{i-1}, g) = \min_{\boldsymbol{\theta} \in \mathbb{R}^N} \mathcal{L}_{\mathcal{T}}^i(v(\cdot; \boldsymbol{\theta}); u_{i-1}, g)$$

for  $i = 1, \dots, m_0$ .

**6. Numerical Experiments.** In this section, we present numerical results for several one dimensional benchmark test problems of scalar nonlinear hyperbolic conservation laws including: (1) the inviscid Burgers equation, i.e.,  $\mathbf{f}(u) = \frac{1}{2}u^2$  (Section 6.1-6.3); (2)  $\mathbf{f}(u) = \frac{1}{4}u^4$  (Section 6.4); and (3) non-convex flux  $\mathbf{f}(u) = \frac{1}{3}u^3$  (Section 6.5).

For any one dimensional nonlinear test problems defined on  $\Omega = (a, b) \times (0, T)$ , we employ the block space-time FV-LSNN method described in the previous section. Specifically, let

$$(6.1) \quad \Omega_i = (a, b) \times \left(0, \frac{iT}{m_0}\right) \quad \text{for } i = 1, \dots, m_0.$$

Then the  $i^{\text{th}}$  space-time block is defined as

$$\Omega_{i-1, i} = \Omega_i \setminus \Omega_{i-1} = (a, b) \times \left(\frac{(i-1)T}{m_0}, \frac{iT}{m_0}\right).$$

Unless otherwise stated, the block  $\Omega_{i-1, i}$  is partitioned into identical squares with size  $h = 0.01$  as the integration mesh  $\mathcal{T}$ ; the boundary integrals in (3.1) are approximated by the composite trapezoidal rule (3.2) with  $\hat{m} = \hat{n} = 2$ , i.e., each control surface is partitioned into two uniform sub-intervals. The minimization problem in (5.2) is numerically solved using the Adams version of gradient descent [19] with either a fixed or an adaptive learning rate.

In order to accurately approximate the discontinuous solution, at least a three-layer neural network is needed, as shown in [4], and hence a three-layer network model is adopted for all test problems in this paper. For the block space-time FV-LSNN method, the same network structure is applied for all blocks  $\Omega_{i-1, i}$  for  $i = 1, \dots, m_0$ . The parameters of the network model for the current block are initialized using those of the previous block as proposed in Remark 4.1 of [5]. To initialize the network in the first block  $\Omega_{0, 1}$ , the parameters of the second hidden layer are randomly generated; and the initialization of the first hidden layer is set up such that an uniform physical partition of the domain is obtained (see [5] and [21] for more details). Additionally, our numerical results suggest that adding a weight  $\alpha$  to the  $L^2$  loss of the initial condition makes the LSNN method easier to train. In the implementation, the following least-squares functional is used:

$$(6.2) \quad \mathcal{L}^i(v; u_{i-1}, g) = \|\nabla \cdot \mathbf{f}(v)\|_{0, \Omega_{i-1, i}}^2 + \alpha \|v - u_{i-1}\|_{0, \Gamma_{i-1, i}}^2 + \|v - g\|_{0, \Gamma_{i-}}^2 \quad \text{for } i = 1, \dots, m_0$$

and the weight  $\alpha$  is empirically chosen.

Let  $u_i$  be the solution of the problem in (5.1) and  $u_{i, \mathcal{T}}$  be the corresponding NN approximation. The network structure is expressed as  $2-n_1-n_2-1$  for a three-layer network with  $n_1$  and  $n_2$  neurons in the respective first and second layers, and so on. The traces of the exact and numerical solutions are depicted on a plane of given time. Those traces accurately show the capability of the numerical approximation in resolving the shock/rarefaction.

**6.1. Riemann problem for the inviscid Burgers equation.** For the one dimensional inviscid Burgers equation,  $f(u) = \frac{1}{2}u^2$ , we report numerical results for the corresponding Riemann problem where the initial condition is given by

$$(6.3) \quad u_0(x) = \begin{cases} u_L, & \text{if } x \leq 0, \\ u_R, & \text{if } x \geq 0. \end{cases}$$

**6.1.1. Shock formation.** The first test problem is the Riemann problem with

$$u_L = 1 > 0 = u_R$$

defined on a computational domain  $\Omega = (-1, 1) \times (0, 0.6)$ . The inflow boundary is

$$\Gamma_- = \Gamma_-^L \cup \Gamma_-^R \equiv \{(-1, t) : t \in [0, 0.6]\} \cup \{(1, t) : t \in [0, 0.6]\}$$

with the boundary conditions:  $g = u_L = 1$  on  $\Gamma_-^L$  and  $g = u_R = 0$  on  $\Gamma_-^R$ .

For this problem, the characteristic lines intersect immediately at  $t \geq 0$  and a shock forms. The weak solution is given by

$$(6.4) \quad u(x, t) = \begin{cases} u_L, & \text{if } x \leq st \\ u_R, & \text{if } x \geq st \end{cases} = \begin{cases} 1, & \text{if } x \leq st, \\ 0, & \text{if } x \geq st \end{cases}$$

with the shock speed determined by the RH condition

$$s = \frac{f(u_L) - f(u_R)}{u_L - u_R} = \frac{f(1) - f(0)}{1 - 0} = 1/2.$$

The block space-time FV-LSNN method using a 2-10-10-1 network is implemented with  $m_0 = 3$  blocks, weight  $\alpha = 20$ , a fixed learning rate 0.003, and 30000 iterations for each block. The relative errors in the  $L^2$  norm are reported in Table 6.1. Traces of the exact solution and numerical approximation on the planes  $t = iT/m_0$  for  $i = 1, \dots, m_0$  are depicted in Fig. 6.1(b)-(d), which clearly indicate that the FV-LSNN method is capable of capturing the shock formation and its speed. Moreover, it approximates the solution well without oscillations.

TABLE 6.1  
Relative  $L^2$  errors of Riemann problem (shock) for Burgers equation

Network structure	Block	$\frac{\ u_i - u_{i,\tau}\ _0}{\ u_i\ _0}$
2-10-10-1	$\Omega_{0,1}$	0.048774
	$\Omega_{1,2}$	0.046521
	$\Omega_{2,3}$	0.044616

**6.1.2. Rarefaction waves.** The second test problem is the Riemann problem with

$$u_L = 0 < 1 = u_R$$

defined on a computational domain  $\Omega = (-1, 2) \times (0, 0.4)$ . The inflow boundary is

$$\Gamma_- = \Gamma_-^L \cup \Gamma_-^R \equiv \{(-1, t) : t \in [0, 0.4]\} \cup \{(2, t) : t \in [0, 0.4]\}$$

with the boundary conditions:  $g = 0$  on  $\Gamma_-^L$  and  $g = 1$  on  $\Gamma_-^R$ .

For this problem, the range of influence of all points in  $\mathbb{R}$  is a proper subset of  $\mathbb{R} \times [0, \infty)$ . Hence, the weak solution of the scalar hyperbolic conservation law is not unique. To ensure the underlying

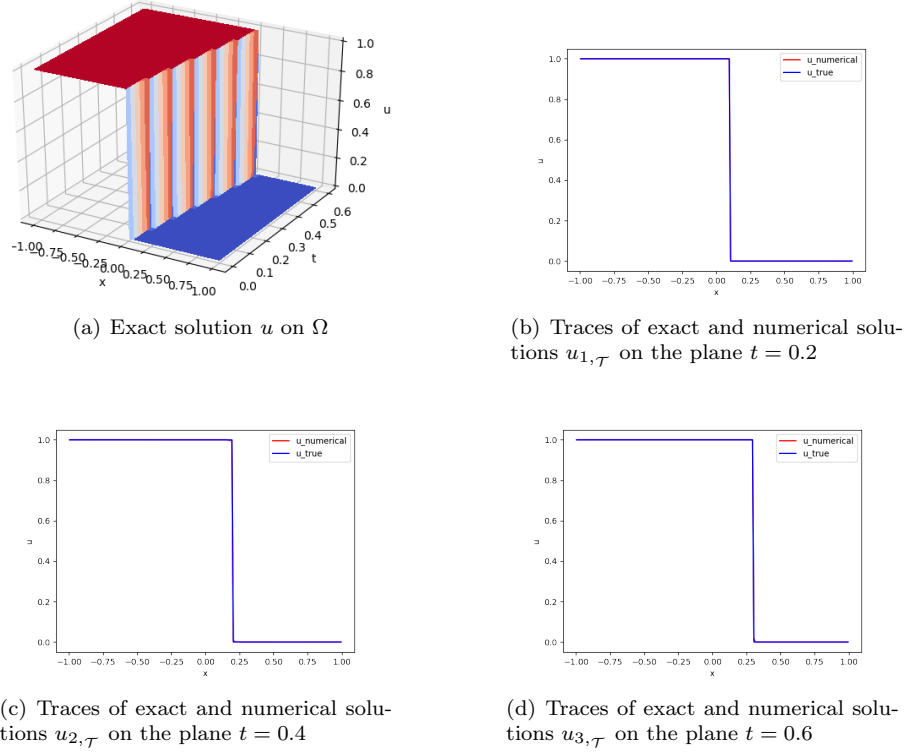


FIG. 6.1. Approximation results of Riemann problem (shock) for Burgers' equation

Cauchy problem having a unique solution over the whole domain  $\mathbb{R} \times [0, \infty)$ , the so-called vanishing viscosity weak solution is introduced (see, e.g., [20, 27]) and given by

$$u(x, t) = \begin{cases} u_L, & \text{if } x < u_L t \\ x/t, & \text{if } u_L t \leq x \leq u_R t \\ u_R, & \text{if } x > u_R t \end{cases} = \begin{cases} 0, & \text{if } x < 0, \\ x/t, & \text{if } 0 \leq x \leq t, \\ 1, & \text{if } x > t. \end{cases}$$

As shown in section 5.1.2 of [5], Roe's scheme has a limitation to resolve the rarefaction by implementing the block space-time conservative LSNN method. Using the same test problem as in [5], we present the results generated by the LS-LSNN method with  $m_0 = 2$  blocks, weights  $\alpha = 10$ , a fixed learning rate 0.003 and 40000 iterations for each block.

The numerical approximation results are reported in Table 6.2. Traces of the exact solution and numerical approximation on the planes  $t = T/2$  and  $t = T$  are depicted in Fig. 6.2. This results show the FV-LSNN method is able to compute physical solution without any extra treatment.

TABLE 6.2  
Relative  $L^2$  errors of Riemann problem (rarefaction) for Burgers equation

Network structure	Block	$\frac{\ u_i - u_{i,\tau}\ _0}{\ u_i\ _0}$
2-10-10-1	$\Omega_{0,1}$	0.013387
	$\Omega_{1,2}$	0.010079

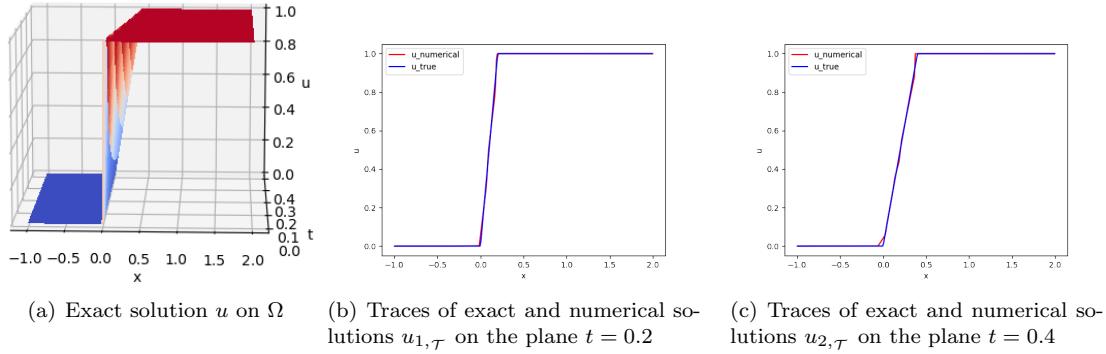


FIG. 6.2. Approximation results of Riemann problem (rarefaction) for Burgers' equation

**6.2. Inviscid Burgers equation with smooth initial conditions.** In [5], we introduced the conservative LSNN method using either the Roe or ENO flux for solving nonlinear hyperbolic conservation laws. The goal of this experiment is to compare the numerical performance of the proposed finite volume with the previous conservative LSNN methods. To this end, we use the same test problem as in Section 5.2 of [5], i.e., the inviscid Burgers equation defined on the computational domain  $\Omega = (0, 2) \times (0, 0.4)$  with a sinusoidal initial condition

$$u_0(x) = 0.5 + \sin(\pi x).$$

and the inflow boundary

$$\Gamma_- = \Gamma_-^L \cup \Gamma_-^R \equiv \{(0, t) : t \in [0, 0.4]\} \cup \{(2, t) : t \in [0, 0.4]\}.$$

The shock of the problem appears at  $t = 1/\pi \approx 0.318$ .

Since the solution of this problem is implicitly given, to accurately measure the quality of NN approximations, a benchmark reference solution  $\hat{u}$  is generated using the traditional mesh-based method. In particular, the third-order accurate WENO scheme [24] and the fourth-order Runge-Kutta method are employed for the respective spatial and temporal discretizations with a fine mesh ( $\Delta x = 0.001$  and  $\Delta t = 0.0002$ ) on the computational domain  $\Omega$ .

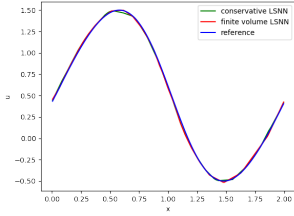
The FV-LSNN method is implemented with the same set of hyper parameters as in Section 5.2 of [5], i.e.,  $m_0 = 8$  blocks, training weight  $\alpha = 5$  and an adaptive learning rate which starts with 0.005 and reduces by half for every 25000 iterations. On each time block, the total number of iterations is set as 50000 and the size of the NN model is 2-30-30-1. Although we observe some error accumulation when the block evolves for both methods, the finite volume method performs better than the conservative method using ENO flux in terms of the relative  $L^2$  norm (see Table 6.3). From the graphical plot, it can also be observed that near the left side of the interface, the FV-LSNN method generate approximations closer to the reference solution (see Fig. 6.3). Computationally, our finite volume scheme is more efficient than the ENO scheme since the former is a linear process while the latter is a nonlinear one.

**6.3. Inviscid Burgers equation with piece-wise linear initial condition.** As pointed out in Sections 3 and 4 that there are two integration error sources when using the FV-LSNN method: one is resulting from the numerical integration of the least-squares functional (4.4) based on a partition  $\mathcal{T}$  of the domain; the other occurs due to the approximation of the boundary integrals in (3.1) by using either the composite trapezoidal (3.2) or the mid-point (3.3) rule. In this section, we focus on analyzing the effect of integration mesh size of  $\mathcal{T}$ .

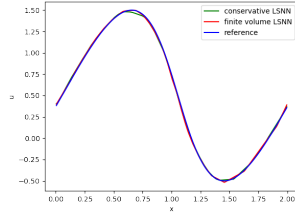
Specifically, we use the inviscid Burgers equation defined on the computational domain  $\Omega =$

TABLE 6.3  
Relative  $L^2$  errors of Burgers equation with a sinusoidal initial condition

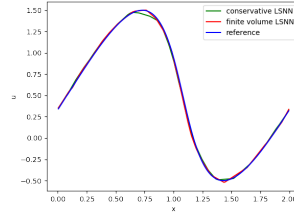
Network structure	Block	FV-LSNN $\frac{\ u_i - u_{i,\mathcal{T}}\ _0}{\ u_i\ _0}$	Conservative LSNN [5] $\frac{\ u_i - u_{i,\mathcal{T}}\ _0}{\ u_i\ _0}$
2-30-30-1	$\Omega_{0,1}$	0.010641	0.010461
	$\Omega_{1,2}$	0.011385	0.012517
	$\Omega_{2,3}$	0.012541	0.019772
	$\Omega_{3,4}$	0.014351	0.022574
	$\Omega_{4,5}$	0.016446	0.029011
	$\Omega_{5,6}$	0.018634	0.038852
	$\Omega_{6,7}$	0.031103	0.075888
	$\Omega_{7,8}$	0.053114	0.078581



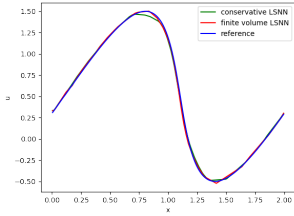
(a) Traces of reference and numerical solutions  $u_{1,\mathcal{T}}$  on the plane  $t = 0.05$



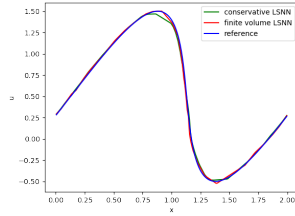
(b) Traces of reference and numerical solutions  $u_{2,\mathcal{T}}$  on the plane  $t = 0.1$



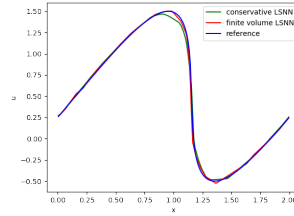
(c) Traces of reference and numerical solutions  $u_{3,\mathcal{T}}$  on the plane  $t = 0.15$



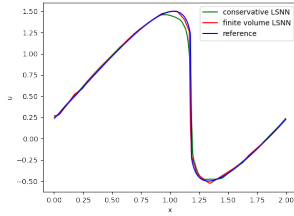
(d) Traces of reference and numerical solutions  $u_{4,\mathcal{T}}$  on the plane  $t = 0.2$



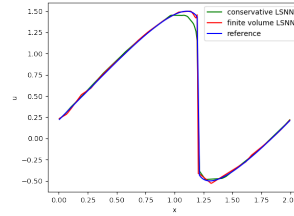
(e) Traces of reference and numerical solutions  $u_{5,\mathcal{T}}$  on the plane  $t = 0.25$



(f) Traces of reference and numerical solutions  $u_{6,\mathcal{T}}$  on the plane  $t = 0.3$



(g) Traces of reference and numerical solutions  $u_{7,\mathcal{T}}$  on the plane  $t = 0.35$



(h) Traces of reference and numerical solutions  $u_{8,\mathcal{T}}$  on the plane  $t = 0.4$

FIG. 6.3. Approximation results of Burgers' equation with a sinusoidal initial condition

$(-1, 2) \times (0, 0.6)$  with a continuous piece-wise linear initial condition

$$u_0(x) = \begin{cases} 1, & \text{if } x < 0, \\ 1 - 2x, & \text{if } 0 \leq x \leq 1/2, \\ 0, & \text{if } x > 1/2. \end{cases}$$

The inflow boundary is

$$\Gamma_- = \Gamma_-^L \cup \Gamma_-^R \equiv \{(-1, t) : t \in [0, 0.6]\} \cup \{(2, t) : t \in [0, 0.6]\}$$

with the boundary conditions:  $g = 1$  on  $\Gamma_-^L$  and  $g = 0$  on  $\Gamma_-^R$ . The exact solution of the test problem is continuous for  $t < 1/2$  and discontinuous for  $t > 1/2$  which is given by

$$u(x, t) = \begin{cases} 1, & \text{if } x < t < \frac{1}{2}, \\ \frac{1 - 2x}{1 - 2t}, & \text{if } t \leq x \leq \frac{1}{2}, \\ 0, & \text{if } x > \frac{1}{2}, \end{cases} \text{ for } t < \frac{1}{2} \text{ and } u(x, t) = \begin{cases} 1, & \text{if } x < \frac{2t + 1}{4}, \\ 0, & \text{if } x \geq \frac{2t + 1}{4}. \end{cases} \text{ for } t > \frac{1}{2}.$$

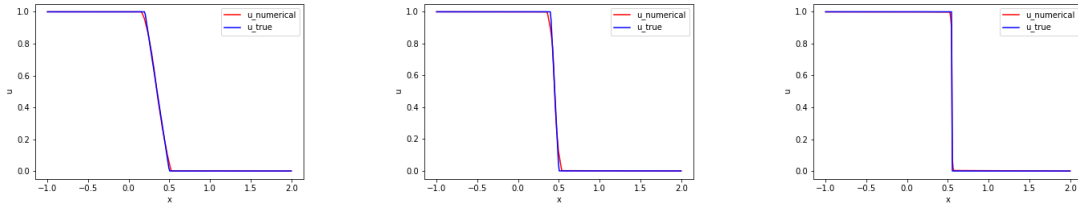
The block space-time FV-LSNN method is implemented with  $m_0 = 6$  blocks,  $\alpha = 10$  in (6.2) and an adaptive learning rate which starts with 0.004 and decays by half for every 10000 iterations. In the training, the total number of the iterations is not limited as to fully explore the network approximation power. Particularly, the following stopping criterion is used with the gradient descent optimizer: the iteration terminates when the relative change of the loss function (6.2) is less than 0.1% in the last 2000 iterations. In addition, a fixed number of sub-intervals  $\hat{m} = \hat{n} = 2$  is used with the composite trapezoidal rule (3.2) to evaluate the boundary integrals in (3.1). Starting with the same initialization for both layers of the 2-10-10-1 NN model, the relative  $L^2$  errors on uniform meshes with different mesh size  $h$  are reported in Table 6.4.

Similar as the observation in Section 5.4 of [5] that the error decreases as the integration mesh becomes finer. However, when the mesh size is small enough, the decreasing rate becomes slow. To accurately evaluate the discrete LS functional (4.7), Table 6.4 indicates that the integration mesh with size  $h = 0.01$  is fine enough for the fixed 2-10-10-1 NN model. Moreover, as depicted in Fig. 6.4, the LSNN method using  $h = 0.01$  is capable of approximating the solution well and resolving the discontinuous interface.

TABLE 6.4  
Relative  $L^2$  errors of the problem with a piece-wise linear initial using different integration mesh sizes

Time block	Integration mesh size				
	$h = 0.1$	$h = 0.05$	$h = 0.025$	$h = 0.01$	$h = 0.005$
$\Omega_{0,1}$	0.012786	0.010261	0.008626	0.006052	0.005145
$\Omega_{1,2}$	0.017806	0.016652	0.013337	0.010296	0.009477
$\Omega_{2,3}$	0.018931	0.014752	0.015185	0.014036	0.013313
$\Omega_{3,4}$	0.036016	0.019801	0.018521	0.015701	0.016125
$\Omega_{4,5}$	0.074236	0.038546	0.038546	0.035891	0.032067
$\Omega_{5,6}$	0.080682	0.049391	0.047908	0.038003	0.035249

**6.4. Riemann problem with  $f(u) = \frac{1}{4}u^4$ .** The goals of this set of numerical experiments are twofold. First, we compare the performance of the composite trapezoidal (3.2) and mid-point (3.3) rules in the FV-LSNN method. Second, we investigate the impact of the number of sub-intervals of the composite quadrature rule on the accuracy of the FV-LSNN method.

(a) Traces of exact and numerical solutions  $u_{2,\mathcal{T}}$  on the plane  $t = 0.2$ (b) Traces of exact and numerical solutions  $u_{4,\mathcal{T}}$  on the plane  $t = 0.4$ (c) Traces of exact and numerical solutions  $u_{6,\mathcal{T}}$  on the plane  $t = 0.6$ FIG. 6.4. Numerical results of Burgers equation with a piece-wise linear initial and integration mesh size  $h = 0.01$ 

To this end, we use the Riemann problem with a convex flux  $\mathbf{f}(u) = f(u) = \frac{1}{4}u^4$  and the initial condition

$$u_L = 1 > 0 = u_R$$

in (6.3). The weak solution of this test problem is given by (6.4) with the shock speed  $s = 1/4$ . The computational domain is chosen to be  $\Omega = (-1, 1) \times (0, 0.4)$  with the inflow boundary

$$\Gamma_- = \Gamma_-^L \cup \Gamma_-^R \equiv \{(-1, t) : t \in [0, 0.4]\} \cup \{(1, t) : t \in [0, 0.4]\}.$$

The inflow boundary conditions are given by  $g = 1$  on  $\Gamma_-^L$  and  $g = 0$  on  $\Gamma_-^R$ .

Adopted the same stopping criterion for the iterative solver as in Section 6.3, the block space-time FV-LSNN method is equipped with  $m_0 = 2$  blocks, the cost function weight  $\alpha = 20$ , a fixed learning rate 0.003 for the first 30000 iterations and 0.001 for the remaining. Setting the network structure of size 2-10-10-1, a uniform fine integration mesh  $\mathcal{T}$  with size  $h = 0.01$  is used to accurately evaluate the functional. The approximation errors generated by different number of sub-intervals using the composite trapezoidal and mid-point rules are reported in Table 6.5 and 6.6, respectively; and graphical results are presented in Fig. 6.5.

Numerical results show that the number of sub-intervals plays an important role for the FV-LSNN method, especially for problems with fluxes other than the quadratic one. It is easy to see its impact on the accuracy of the FV-LSNN method, but also it might affect the training of NN: possibly trapped at a local minimum and hence failed to resolve the discontinuity (see Fig. 6.5) when  $\hat{m} = \hat{n} = 2$ . As the number of sub-intervals increases, the FV-LSNN approximation is very accurate and almost matches the exact solution. Since the accuracy of the FV-LSNN method depends on both the approximation accuracy of the NN and the FVA, the second and third columns of Table 6.5 and 6.6 show that a large number of sub-intervals does not necessarily improve much accuracy of the FV-LSNN. Finally, there is no big observable difference between the composite trapezoidal and mid-point rules in the FV-LSNN method as they generate similar results.

TABLE 6.5  
Relative  $L^2$  errors of the problem with  $f(u) = \frac{1}{4}u^4$  using different number of sub-intervals in the composite trapezoidal rule (3.2)

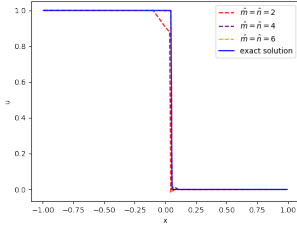
Time block	Number of sub-intervals		
	$\hat{m} = \hat{n} = 2$	$\hat{m} = \hat{n} = 4$	$\hat{m} = \hat{n} = 6$
$\Omega_{0,1}$	0.067712	0.010446	0.004543
$\Omega_{1,2}$	0.108611	0.008275	0.009613



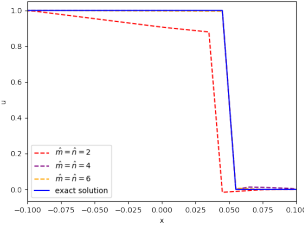
TABLE 6.6

Relative  $L^2$  errors of the problem with  $f(u) = \frac{1}{4}u^4$  using different number of sub-intervals in the composite mid-point rule (3.3)

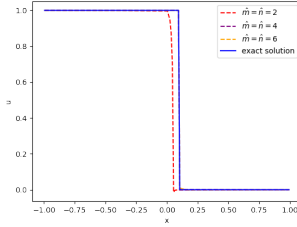
Time block	Number of sub-intervals		
	$\hat{m} = \hat{n} = 2$	$\hat{m} = \hat{n} = 4$	$\hat{m} = \hat{n} = 6$
$\Omega_{0,1}$	0.096238	0.007917	0.003381
$\Omega_{1,2}$	0.159651	0.007169	0.005028



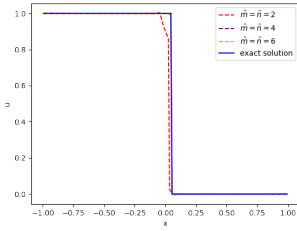
(a) Traces of exact and numerical solutions  $u_{1,\mathcal{T}}$  using the trapezoidal rule on the plane  $t = 0.2$



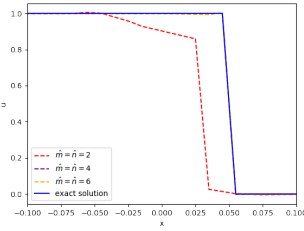
(b) Zoom-in plot near the discontinuous interface of sub-figure (a)



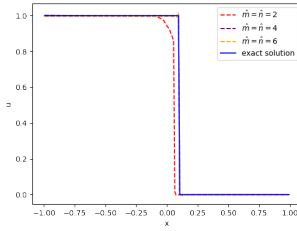
(c) Traces of exact and numerical solutions  $u_{2,\mathcal{T}}$  using the trapezoidal rule on the plane  $t = 0.4$



(d) Traces of exact and numerical solutions  $u_{1,\mathcal{T}}$  using the mid-point rule on the plane  $t = 0.2$



(e) Zoom-in plot near the discontinuous interface of sub-figure (d)



(f) Traces of exact and numerical solutions  $u_{2,\mathcal{T}}$  using the mid-point rule on the plane  $t = 0.4$

FIG. 6.5. Numerical results of the problem with  $f(u) = \frac{1}{4}u^4$  using the composite trapezoidal and mid-point rules

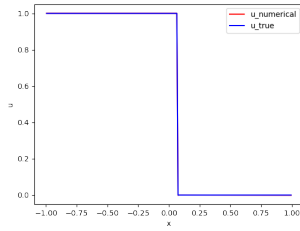
**6.5. Riemann problem with a non-convex flux**  $f(u) = \frac{1}{3}u^3$ . The last test problem is a modification of the previous one by replacing the convex flux by a non-convex flux  $f(u) = \frac{1}{3}u^3$ . Its weak solution is given in (6.4) with the shock speed  $s = 1/3$ .

The block space-time FV-LSNN method is employed with a 2-10-10-1 network. A same set of hyper parameters as in Section 6.4 is used except that a learning rate 0.003 is fixed throughout the 30000 iterations for each block. To evaluate the boundary integrals in (3.1),  $\hat{m} = \hat{n} = 6$  are used in the composite trapezoidal rule (3.2). Since the second hidden layer parameters in the network are randomly generated, the experiment is replicated 10 times. In most of the duplicate runs, similar results are obtained as the best result reported in Table 6.7 and Fig. 6.6 (a)-(c). This indicates that the FV-LSNN method can capture the discontinuous interface for non-convex flux problems as well. However, one out of ten runs produce slightly inferior results depicted in Fig. 6.6 (d) and (e). At this stage, we think that those results are due to the random initialization in training non-convex optimization. This issue would be resolved through the adaptive network enhancement (ANE) method in [21, 6], which eliminates the random initialization and utilizes the

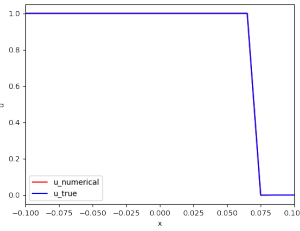
method of continuation for obtaining a good initial in training. Moreover, the ANE method is able to produce a relatively small neural network for the underlying problem. Work along this direction will be pursued in the forthcoming paper.

TABLE 6.7  
Relative  $L^2$  errors of Riemann problem with a non-convex flux  $f(u) = \frac{1}{3}u^3$

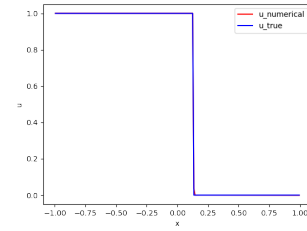
Network structure	Block	$\frac{\ u_i - u_{i,\tau}\ _0}{\ u_i\ _0}$
2-10-10-1	$\Omega_{0,1}$	0.000918
	$\Omega_{1,2}$	0.002514



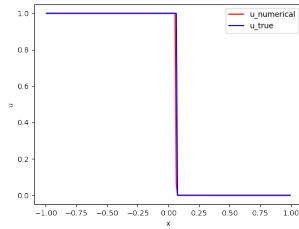
(a) Traces of exact and numerical solutions  $u_{1,\tau}$  on the plane  $t = 0.2$



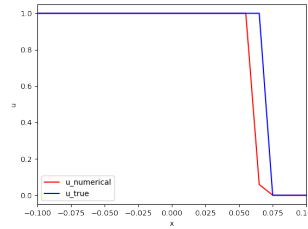
(b) Zoom-in plot near the discontinuous interface of sub-figure (a)



(c) Traces of exact and numerical solutions  $u_{2,\tau}$  on the plane  $t = 0.4$



(d) Traces of exact and numerical solutions  $u_{1,\tau}$  on the plane  $t = 0.2$



(e) Zoom-in plot near the discontinuous interface of sub-figure (d)

FIG. 6.6. Numerical results of Riemann problem with a non-convex flux  $f(u) = \frac{1}{3}u^3$

**7. Discussion and Conclusion.** This paper introduces and studies a finite volume least-squares ReLU neural network (FV-LSNN) method for solving scalar nonlinear hyperbolic conservation laws. As seen in [4, 5], with the simplest LS formulation, approximating the differential operator well in the LS functional is essential for the success of the space-time LSNN method. In this paper, we introduce a new finite volume approximation (FVA) to the divergence operator. The FVA is constructed through the Gauss divergence theorem and hence enforces the RH relation weakly. Accuracy of the FVA, even for the discontinuous solution, is guaranteed by the number of integration points of the composite trapezoidal/mid-point rule. Comparing to existing nonlinear conservative schemes, the FVA is a linear process and hence simpler and efficient.

The FV-LSNN method based on the newly developed FVA using the trapezoidal rule is tested for the inviscid Burgers equation with various initial conditions: Riemann problems with shock formation and rarefaction waves, smooth and piece-wise linear data. For all test problems, numerical results demonstrate that the FV-LSNN method is capable of computing the physical solution

for problems with rarefaction waves and capturing shocks accurately without oscillation, and is more accurate than the LSNN using the Roe and the second-order ENO schemes. For the Riemann problems with convex  $f(u) = u^4/4$  and non-convex  $f(u) = u^3/3$  fluxes, numerical results demonstrate the same capacity of the FV-LSNN method provided that a *composite* trapezoidal or mid-point rule with at least 4 sub-intervals is used.

The number of degrees of freedom of the FV-LSNN method is significantly smaller than those of traditional mesh-based numerical methods. However, it is computationally intensive and complicated to train the neural network. For a network with more than one hidden layer, random initialization of the parameters in layers beyond the first hidden layer would cause some uncertainty in training NN (iteratively solving the resulting non-convex optimization) as observed in Section 6.5. This issue plus designation of a proper architecture of NN would be addressed in a forthcoming paper using the adaptive network enhancement (ANE) method newly developed in [21, 6].

## REFERENCES

- [1] P. Bochev and J. Choi. Improved least-squares error estimates for scalar hyperbolic problems. *Computational Methods in Applied Mathematics*, 1(2):115–124, 2001.
- [2] F. Brezzi, L. D. Marini, and E. Süli. Discontinuous galerkin methods for first-order hyperbolic problems. *Mathematical models and methods in applied sciences*, 14(12):1893–1903, 2004.
- [3] E. Burman. A posteriori error estimation for interior penalty finite element approximations of the advection-reaction equation. *SIAM journal on numerical analysis*, 47(5):3584–3607, 2009.
- [4] Z. Cai, J. Chen, and M. Liu. Least-squares ReLU neural network (LSNN) method for linear advection-reaction equation. *Journal of Computational Physics*, 443:110514, 2021.
- [5] Z. Cai, J. Chen, and M. Liu. Least-squares ReLU neural network (LSNN) method for scalar nonlinear hyperbolic conservation law. *arXiv preprint arXiv:2105.11627v1*, 2021.
- [6] Z. Cai, J. Chen, and M. Liu. Self-adaptive deep neural network: Numerical approximation to functions and pdes. *Journal of Computational Physics*, submitted, 2021.
- [7] Z. Cai, J. Chen, M. Liu, and X. Liu. Deep least-squares methods: An unsupervised learning-based numerical method for solving elliptic PDEs. *Journal of Computational Physics*, 420:109707, 2020.
- [8] W. Dahmen, C. Huang, C. Schwab, and G. Welper. Adaptive petrov–galerkin methods for first order transport equations. *SIAM journal on numerical analysis*, 50(5):2420–2445, 2012.
- [9] H. De Sterck, T. A. Manteuffel, S. F. McCormick, and L. Olson. Least-squares finite element methods and algebraic multigrid solvers for linear hyperbolic pdes. *SIAM Journal on Scientific Computing*, 26(1):31–54, 2004.
- [10] H. De Sterck, T. A. Manteuffel, S. F. McCormick, and L. Olson. Numerical conservation properties of H(div)-conforming least-squares finite element methods for the burgers equation. *SIAM Journal on Scientific Computing*, 26(5):1573–1597, 2005.
- [11] L. Demkowicz and J. Gopalakrishnan. A class of discontinuous petrov–galerkin methods. part i: The transport equation. *Computer Methods in Applied Mechanics and Engineering*, 199(23-24):1558–1572, 2010.
- [12] E. Godlewski and P.-A. Raviart. *Numerical approximation of hyperbolic systems of conservation laws*, volume 118. Springer Science & Business Media, 2013.
- [13] D. Gottlieb and C.-W. Shu. On the gibbs phenomenon and its resolution. *SIAM review*, 39(4):644–668, 1997.
- [14] J. S. Hesthaven. *Numerical methods for conservation laws: From analysis to algorithms*. SIAM, 2017.
- [15] J. S. Hesthaven and T. Warburton. *Nodal discontinuous Galerkin methods: algorithms, analysis, and applications*. Springer Science & Business Media, 2007.
- [16] P. Houston, J. A. Mackenzie, E. Süli, and G. Warnecke. A posteriori error analysis for numerical approximations of friedrichs systems. *Numerische Mathematik*, 82(3):433–470, 1999.
- [17] P. Houston, R. Rannacher, and E. Süli. A posteriori error analysis for stabilised finite element approximations of transport problems. *Computer methods in applied mechanics and engineering*, 190(11-12):1483–1508, 2000.
- [18] D. Z. Kalchev and T. A. Manteuffel. A least-squares finite element method based on the helmholtz decomposition for hyperbolic balance laws. *arXiv preprint arXiv:1911.05831v2*, 2020.
- [19] D. P. Kingma and J. Ba. Adam: A method for stochastic optimization. In *International Conference on Representation Learning, San Diego*, 2015.
- [20] R. J. LeVeque and R. J. LeVeque. *Numerical methods for conservation laws*, volume 132. Springer, 1992.
- [21] M. Liu, Z. Cai, and J. Chen. Adaptive two-layer ReLU neural network. *arXiv preprint arXiv:2107.08935v1*, 2021.
- [22] M. Raissi, P. Perdikaris, and G. E. Karniadakis. Physics-informed neural networks: A deep learning framework for solving forward and inverse problems involving nonlinear partial differential equations. *Journal of Computational Physics*, 378:686–707, 2019.

- [23] P. L. Roe. Approximate riemann solvers, parameter vectors, and difference schemes. *Journal of computational physics*, 43(2):357–372, 1981.
- [24] C.-W. Shu. Essentially non-oscillatory and weighted essentially non-oscillatory schemes for hyperbolic conservation laws. In *Advanced numerical approximation of nonlinear hyperbolic equations*, pages 325–432. Springer, 1998.
- [25] C.-W. Shu and S. Osher. Efficient implementation of essentially non-oscillatory shock-capturing schemes. *Journal of computational physics*, 77(2):439–471, 1988.
- [26] J. Sirignano and K. Spiliopoulos. DGM: A deep learning algorithm for solving partial differential equations. *Journal of Computational Physics*, 375:1139–1364, 2018.
- [27] J. W. Thomas. *Numerical partial differential equations: finite difference methods*, volume 22. Springer Science & Business Media, 2013.

**8. Appendix.** In the appendix, we provide proof of Lemmas 3.2 and 3.3. To this end, denote the integral, the trapezoidal rule, and the mid-point rule of a function  $\varphi$  over an interval  $[0, \rho]$  by

$$I(\varphi) = \int_0^\rho \varphi(s) ds, \quad Q_t(\varphi) = \frac{\rho}{2}(\varphi(0) + \varphi(\rho)), \quad \text{and} \quad Q_m(\varphi) = \rho\varphi(\rho/2),$$

respectively. Let  $p, q \in (1, \infty]$  such that  $1/p + 1/q = 1$ . Assume that  $\varphi$  is a  $C^2(0, \rho)$  function, then it is easy to show the following error bounds:

$$(8.1) \quad |I(\varphi) - Q_{int}(\varphi)| \leq \begin{cases} C\rho^{2+1/q}\|\varphi''\|_{L^p(0,\rho)}, & \text{for } int = t, m. \\ C\rho^{1+1/q}\|\varphi'\|_{L^p(0,\rho)} \end{cases}$$

*Proof of Lemma 3.2.* It follows from (3.1), (3.3), and (8.1) that

$$\begin{aligned} & \|\nabla_\tau^m \cdot \mathbf{f}(u) - \text{avg}(\nabla \cdot \mathbf{f}(u))\|_{L^p(K_{ij})} = |K_{ij}|^{1/p} \left| \text{avg}_{K_{ij}}(\nabla \cdot \mathbf{f}(u)) - \nabla_\tau^m \cdot \mathbf{f}(u(\mathbf{m}_{K_{ij}})) \right| \\ &= \frac{1}{|K_{ij}|^{1/q}} \left| \sum_{k=0}^{\hat{n}-1} \left\{ \int_{t_j^k}^{t_j^{k+1}} (\sigma(x_{i+1}, t) - \sigma(x_i, t)) dt - \hat{\tau} \left( \sigma(x_{i+1}, t_j^{k+1/2}) - \sigma(x_i, t_j^{k+1/2}) \right) \right\} \right. \\ & \quad \left. + \sum_{k=0}^{\hat{m}-1} \left\{ \int_{x_i^k}^{x_i^{k+1}} (u(x, t_{j+1}) - u(x, t_j)) dx - \hat{h} \left( u(x_i^{k+1/2}, t_{j+1}) - u(x_i^{k+1/2}, t_j) \right) \right\} \right| \\ &\leq \frac{C}{|K_{ij}|^{1/q}} \left\{ \sum_{k=0}^{\hat{n}-1} \hat{\tau}^{2+1/q} \|\sigma_{tt}(x_{i+1}, \cdot) - \sigma_{tt}(x_i, \cdot)\|_{L^p(t_j^k, t_j^{k+1})} \right. \\ & \quad \left. + \sum_{k=0}^{\hat{m}-1} \hat{h}^{2+1/q} \|u_{xx}(\cdot, t_{j+1}) - u_{xx}(\cdot, t_j)\|_{L^p(x_i^k, x_i^{k+1})} \right\}, \end{aligned}$$

which, together with the triangle and the Hölder inequalities, implies

$$(8.2) \quad \begin{aligned} & \|\nabla_\tau^{int} \cdot \mathbf{f}(u) - \text{avg}(\nabla \cdot \mathbf{f}(u))\|_{L^p(K_{ij})} \\ &\leq C \left( \frac{\tau^2}{\hat{n}^2 \hat{h}^{1/q}} \sum_{l=i}^{i+1} \|\sigma_{tt}(x_l, \cdot)\|_{L^p(t_j, t_{j+1})} + \frac{h^2}{\hat{m}^2 \tau^{1/q}} \sum_{l=j}^{j+1} \|u_{xx}(\cdot, t_l)\|_{L^p(x_i, x_{i+1})} \right). \end{aligned}$$

Now, (3.5) for the mid-point rule is a direct consequence of the assumption on the smoothness of the solution and the flux. (3.5) for the trapezoidal rule may be proved in a similar fashion. This completes the proof of Lemma 3.2.  $\square$

To prove Lemma 3.3, we first estimate an error bound of numerical integration for piece-wise smooth and discontinuous integrant over interval  $[0, \rho]$ .

LEMMA 8.1. *For any  $0 < \delta < \rho/2$ , assume that  $\varphi \in C^1((0, \delta)) \cap C^1((\delta, \rho))$  is a piece-wise  $C^1$  function. Denote by  $j_\varphi = |\varphi(\delta^+) - \varphi(\delta^-)|$  the jump of  $\varphi(s)$  at  $s = \delta$ . Then there exists a positive constant  $C$  such that*

$$(8.3) \quad |I(\varphi) - Q_t(\varphi)| \leq C\rho^{1+1/q} (\|\varphi'\|_{L^p(0,\delta)} + \|\varphi'\|_{L^p(\delta,\rho)}) + \left|\frac{\rho}{2} - \delta\right| j_\varphi$$

for the trapezoidal rule and that

$$(8.4) \quad |I(\varphi) - Q_m(\varphi)| \leq C\rho^{1+1/q} (\|\varphi'\|_{L^p(0,\delta)} + \|\varphi'\|_{L^p(\delta,\rho)}) + \delta j_\varphi$$

for the mid-point rule.

*Proof.* Denote the linear interpolant of  $\varphi$  on the interval  $[0, \rho]$  by  $\varphi_1(s) = \varphi(0) \frac{\rho-s}{\rho} + \varphi(\rho) \frac{s}{\rho}$ . For any  $s \in (0, \delta)$ , by the fact that  $\varphi(0) - \varphi_1(0) = 0$ , a standard argument on the error bound of interpolant yields that there exists a  $\xi_- \in (0, \delta)$  such that

$$\varphi(s) - \varphi_1(s) = \varphi'(\xi_-)s - \frac{s}{\rho}(\varphi(\rho) - \varphi(0)),$$

which implies

$$\int_0^\delta (\varphi(s) - \varphi_1(s)) ds = \int_0^\delta \varphi'(\xi_-)s ds - \frac{\delta^2}{2\rho} (\varphi(\rho) - \varphi(0)).$$

In a similar fashion, there exists a  $\xi_+ \in (\delta, \rho)$  such that

$$\int_\delta^\rho (\varphi(s) - \varphi_1(s)) ds = \int_\delta^\rho \varphi'(\xi_+)(s - \rho) ds + \frac{(\rho - \delta)^2}{2\rho} (\varphi(\rho) - \varphi(0)).$$

Combining the above inequalities and using the triangle and the Hölder inequalities give

$$\begin{aligned} |I(\varphi) - Q_t(\varphi)| &= \left| \int_0^\delta \varphi'(\xi_-)s ds + \int_\delta^\rho \varphi'(\xi_+)(s - \rho) ds + \frac{\rho - 2\delta}{2} (\varphi(\rho) - \varphi(0)) \right| \\ &\leq \frac{1}{(1+q)^{1/q}} \rho^{1+1/q} (\|\varphi'\|_{L^p(0,\delta)} + \|\varphi'\|_{L^p(\delta,\rho)}) + \left|\frac{\rho}{2} - \delta\right| |\varphi(\rho) - \varphi(0)| \end{aligned}$$

It follows from the triangle and the Hölder inequalities that

$$|\varphi(\rho) - \varphi(0)| \leq \left| \int_\delta^\rho \varphi'(s) ds \right| + \left| \int_0^\delta \varphi'(s) ds \right| + j_\varphi \leq \rho^{1/q} (\|\varphi'\|_{L^p(0,\delta)} + \|\varphi'\|_{L^p(\delta,\rho)}) + j_\varphi$$

Now, the above two inequalities and the fact that  $\left|\frac{\rho}{2} - \delta\right| \leq \frac{\rho}{2}$  imply (8.3).

To prove the validity of (8.4), note that for any  $s \in (0, \delta)$  we have

$$\begin{aligned} \varphi(s) - \varphi(\rho/2) &= \int_{\delta^-}^s \varphi'(s) ds + \int_{\rho/2}^{\delta^+} \varphi'(s) ds + \varphi(\delta^-) - \varphi(\delta^+) \\ &\leq (\delta - s)^{1/q} \|\varphi'\|_{L^p(s,\delta)} + (\rho/2 - \delta)^{1/q} \|\varphi'\|_{L^p(\delta,\rho/2)} + \varphi(\delta^-) - \varphi(\delta^+), \end{aligned}$$

which, together with the triangle inequality, implies

$$\left| \int_0^\delta (\varphi(s) - \varphi(\rho/2)) ds \right| \leq \left(\frac{\rho}{2}\right)^{1+1/q} (\|\varphi'\|_{L^p(0,\delta)} + \|\varphi'\|_{L^p(\delta,\rho/2)}) + \delta j_\varphi.$$

Similarly, we have

$$\left| \int_\delta^\rho (\varphi(s) - \varphi(\rho/2)) ds \right| \leq \frac{2q}{1+q} \left(\frac{\rho}{2}\right)^{1+1/q} \|\varphi'\|_{L^p(\delta,\rho)}.$$

Now, (8.4) follows from the triangle inequality and the above two inequalities. This completes the proof of the lemma.  $\square$

Next, we consider the case that the solution  $u$  is discontinuous on  $\partial K_{ij}$  (the boundary of  $K_{ij}$ ). Without loss of generality, assume that the discontinuous interface  $\Gamma_{ij}$  of  $u$  intercepts two edges of  $\partial K_{ij}$ . Denote by  $\llbracket u \rrbracket_i$  and  $\llbracket u \rrbracket_{i+1}$  the absolute value of jumps of  $u$  on the two horizontal boundary edges,  $t = t_j$  and  $t = t_{j+1}$ , of  $\partial K_{ij}$ , respectively; similarly,  $\llbracket \sigma \rrbracket_j$  and  $\llbracket \sigma \rrbracket_{j+1}$  the absolute value of jumps of  $\sigma$  on the two vertical edges,  $x = x_i$  and  $x = x_{i+1}$ , of  $\partial K_{ij}$ , respectively. Let

$$d_{ij}(\llbracket \sigma \rrbracket, \llbracket u \rrbracket) = \begin{cases} \delta_i^t \llbracket \sigma \rrbracket_i + \delta_{i+1}^t \llbracket \sigma \rrbracket_{j+1}, & \Gamma_{ij} \text{ intercepts two vertical edges,} \\ \delta_j^x \llbracket u \rrbracket_j + \delta_{j+1}^x \llbracket u \rrbracket_{j+1}, & \Gamma_{ij} \text{ intercepts two horizontal edges,} \\ \delta^x \llbracket \sigma \rrbracket_{ij} + \delta^t \llbracket u \rrbracket_{ij}, & \Gamma_{ij} \text{ intercepts one horizontal and one vertical edges,} \end{cases}$$

where  $\llbracket \sigma \rrbracket_{ij} = \max\{\llbracket \sigma \rrbracket_i, \llbracket \sigma \rrbracket_{i+1}\}$ ,  $\llbracket u \rrbracket_{ij} = \max\{\llbracket u \rrbracket_j, \llbracket u \rrbracket_{j+1}\}$ ,  $\delta^x = \max\{\delta_j^x, \delta_{j+1}^x\}$ , and  $\delta^t = \max\{\delta_i^t, \delta_{i+1}^t\}$ ; for  $l = j, j+1$ ,  $\delta_l^x$  is the distance from the discontinuity point on  $\Gamma_{ij} \cap \{t = t_l\}$  to the nearest mid-points  $\{(x_i^{k+1/2}, t_l)\}_{k=0}^{\hat{n}-1}$  and grid points  $\{(x_i^k, t_l)\}_{k=0}^{\hat{n}}$  for the discrete divergence operator  $\nabla_\tau^t \cdot$  and  $\nabla_\tau^m \cdot$ , respectively; for  $l = i, i+1$ ,  $\delta_l^t$  is defined accordingly.

*Proof of Lemma 3.3.* Similar to the proof of Lemma 3.2, the left-hand side of (3.6) may be expressed as the sum of integrals over sub-intervals and their numerical integrations as in the beginning of the proof of Lemma 3.2. Integrals over all sub-intervals except  $(x_i^{k_j}, x_i^{k_j+1})$  and  $(x_i^{k_{j+1}}, x_i^{k_{j+1}+1})$  may be bounded by the first term of (3.6). In a similar fashion, using Lemma 8.1, the integrals over the intervals  $(x_i^{k_l}, x_i^{k_l+1})$  for  $l = j, j+1$  may be bound by the second and third terms in the right-hand side of (3.6).  $\square$